Universiteit Leiden
The Netherlands

Towards fibre-like loss for photonic integration from violet to near-infrared

Chen, H.J.; Colburn, K.; Liu, P., Yan, H.; Hou, H.; Ge, J.; Liu, J.-Y.; ... ; Vahala, K.

Citation
Chen, H. J., Colburn, K., Liu, P. , Y. , H., Hou, H., Ge, J., Liu, J. -Y., ... Vahala, K. (2026). Towards fibre-like loss for photonic integration from violet to near-infrared. *Nature*, *649*, 338-344. doi:10.1038/s41586-025-09889-w

Version: Publisher's Version
License: Creative Commons CC BY-NC-ND 4.0 license
Downloaded from: https://hdl.handle.net/1887/4306931

Note: To cite this publication please use the final published version (if applicable).

Article

Towards fibre-like loss for photonic integration from violet to near-infrared

https://doi.org/10.1038/s41586-025-09889-w

Received: 15 April 2025

Accepted: 10 November 2025

Published online: 7 January 2026

Open access

Check for updates

Hao-Jing Chen[1,5]✉, Kellan Colburn[1,5]✉, Peng Liu[1], Hongrui Yan[1], Hanfei Hou[1], Jinhao Ge[1], Jin-Yu Liu[1], Phineas Lehan[1], Qing-Xin Ji[1], Zhiquan Yuan[1], Dirk Bouwmeester[2,3], Christopher Holmes[4], James Gates[4], Henry Blauvelt[1] & Kerry Vahala[1]✉

Over the past decades, remarkable progress has been made in reducing the loss of photonic integrated circuits (PICs) within the telecom band[1–4], facilitating on-chip applications spanning low-noise optical[5] and microwave synthesis[6], to lidar[7] and photonic artificial intelligence engines[8]. However, several obstacles arise from the marked increase in material absorption and scattering losses at shorter wavelengths[9,10], which prominently elevate power requirements and limit performance in the visible and near-visible spectrum. Here we present an ultralow-loss PIC platform based on germano-silicate—the material underlying the extraordinary performance of optical fibre—but realized by a fully CMOS-foundry-compatible process. These PICs achieve resonator *Q* factors surpassing 180 million from violet to telecom wavelengths. They also attain a 10-dB higher quality factor without thermal treatment in the telecom band, expanding opportunities for heterogeneous integration with active components[11]. Other features of this platform include readily engineered waveguide dispersion, acoustic mode confinement and large-mode-area-induced thermal stability—each demonstrated by soliton microcomb generation, stimulated Brillouin lasing and low-frequency-noise self-injection locking, respectively. The success of these germano-silicate PICs can ultimately enable fibre-like loss onto a chip, leading to an additional 20-dB improvement in waveguide loss over the current highest performance photonic platforms. Moreover, the performance abilities demonstrated here bridge ultralow-loss PIC technology to optical clocks[12], precision navigation systems[13] and quantum sensors[14].

At shorter wavelengths (400–1,100 nm), waveguide losses surge because of two fundamental limitations[9,10]. First, scattering losses increase as the optical wavelength approaches the scale of surface roughness (surface Rayleigh scattering). Second, absorption losses increase as photon energy enters the Urbach tail of amorphous or crystalline dielectrics. However, many important photonic applications operate in these wavelengths[14,15], such as optical clocks, quantum computing and networks, bioimaging, astronomical observation, underwater and data centre communications, compact lidar, and atomic physics studies in general (Fig. 1a). Silica (SiO_2) and germanium-doped silica (germano-silicate or Ge-silica) have been widely adopted in optical fibres for short-wavelength operation because of their exceptionally low material absorption[16]. Nevertheless, because of the need for suspended geometries in the case of silica[17,18], or the lack of well-developed fabrication processes for germano-silicate[19], the promise of fibre-like loss in a photonic integrated circuit (PIC) platform remains untapped.

In this work, we present the first step towards using the materials of fibre optics in achieving planar integrated photonic circuits with fibre-like loss. As in fibre optics, GeO_2 doping elevates the refractive index of the Ge-silica core, enabling optical confinement within a silica cladding. A deep-ultraviolet (DUV) stepper lithography-based manufacturing process is developed to fabricate planar integrated waveguide circuits on silicon wafers. Leveraging the famously low material loss of Ge-silica[16] and the unique low-viscosity reflow properties[20] at standard furnace temperatures, we achieve sub-dB m^{-1} waveguide losses spanning the violet to telecom bands (Fig. 1b). Notably, the waveguide loss in the violet band is 13 dB lower than any current integrated platforms, whereas the lowest loss of 0.08 dB m^{-1} at 1,064 nm reaches a loss level close to the first low-loss optical fibre produced by Corning in 1970 (0.02 dB m^{-1}) (ref. 21). Crucially, ultralow losses without post-processing thermal annealing can be achieved, which is an important enabler for monolithic/heterogeneous integration with temperature-sensitive materials[11].

Beyond its record-low loss performance, several material and practical advantages of this platform are demonstrated. First, the DUV-stepper-defined waveguides are readily dispersion-engineered as required for soliton microcomb generation (demonstrated by soliton microcomb). Second, GeO_2 doping reduces the acoustic velocity

[1]T. J. Watson Laboratory of Applied Physics, California Institute of Technology, Pasadena CA, USA. [2]Department of Physics, University of California Santa Barbara, Santa Barbara CA, USA. [3]Huygens-Kamerlingh Onnes Laboratory, Leiden University, Leiden, The Netherlands. [4]Optoelectronics Research Centre, University of Southampton, Southampton, UK. [5]These authors contributed equally: Hao-Jing Chen, Kellan Colburn. ✉e-mail: haojing@caltech.edu; kcolburn@caltech.edu; vahala@caltech.edu

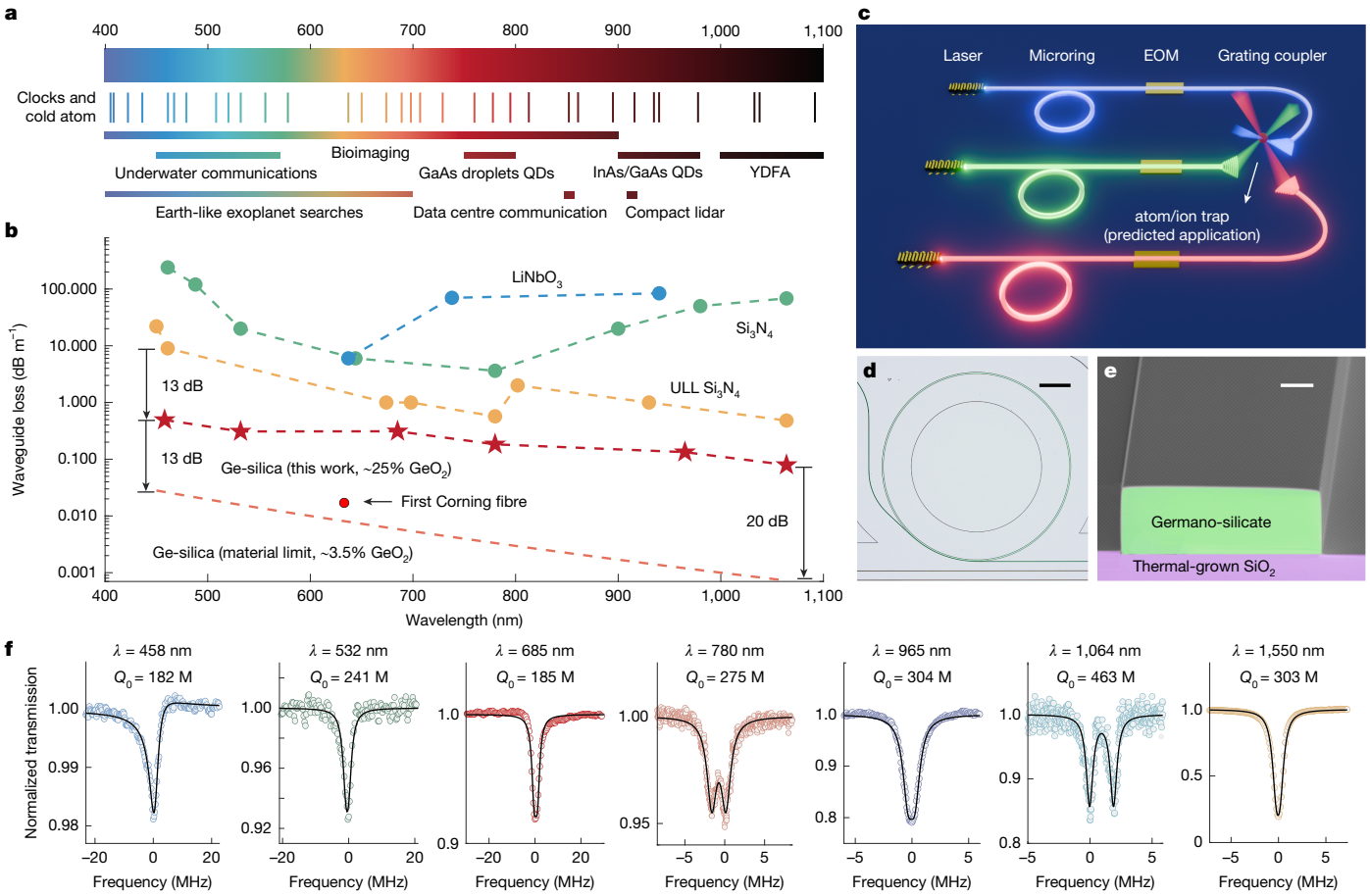

Fig. 1 | Ultrahigh-*Q* germano-silicate device from violet to near IR. a, Spectrum coverage of photonics application in the visible and short-NIR regions[14]. QD, quantum dot; YDFA, Yb-doped fibre amplifier. **b**, Waveguide propagation loss across broadband spectrum of state-of-the-art integrated platforms compared with the present work. Annealed Ge-silica waveguide losses are 0.49 dB m^{-1} at 458 nm, 0.32 dB m^{-1} at 532 nm, 0.32 dB m^{-1} at 685 nm, 0.19 dB m^{-1} at 780 nm, 0.14 dB m^{-1} at 965 nm and 0.08 dB m^{-1} at 1,064 nm, 0.09 dB m^{-1} at 1,550 nm. Unannealed Ge-silica waveguide losses are 1.76 dB m^{-1} at 458 nm, 1.02 dB m^{-1} at 532 nm, 0.56 dB m^{-1} at 685 nm, 0.29 dB m^{-1} at 780 nm, 0.21 dB m^{-1} at 965 nm, and 0.19 dB m^{-1} at 1,064 nm, 0.15 dB m^{-1} at 1,550 nm. Data from refs. 9,36–38 for ULL Si_3N_4; refs. 10,15,39,40 for Si_3N_4; refs. 41–43 for $LiNbO_3$; ref. 16 for the material limit of Ge-silica (standard modern fibre with a GeO_2 content around 3.5 mol%). **c**, Schematic of high-performance visible PICs with multi-material integration for on-chip atom/ion control, consisting of blocks of III–V lasers, Ge-silica microresonators, $LiNbO_3$ electro-optic modulators and vertical grating couplers. **d**, Microscopy image of a Ge-silica microring device. **e**, SEM image of annealed waveguide. **f**, Transmission spectra and corresponding intrinsic *Q* factors (Q_0) of Ge-silica microring resonators at seven wavelengths spanning from violet to NIR. The observed double-dip features at 780 nm and 1,064 nm arise from mode splitting induced by backscattering in the microcavity, whereas the Fano lineshape at 458 nm originates from multimode interference (see detailed analysis in the Supplementary Information). Scale bars, 500 µm (**d**); 2 µm (**e**).

relative to silica, enabling simultaneous confinement of an optical and acoustic mode within the waveguide core (demonstrated by Brillouin lasing). Finally, it can support thicknesses over 4 µm, enabling low thermorefractive noise (TRN) by the generation of a large mode area (LMA) circuit (demonstrated by low-frequency-noise self-injection locking (SIL)). Overall, this platform incorporates essential ingredients of high-performance multi-functionalized visible PICs, including ultralow loss, multi-material integration ability and high noise suppression, thereby paving the way for high-complexity system-level applications such as on-chip atom and ion control[22] (Fig. 1c).

Broadband ultrahigh-*Q* microresonators

To evaluate performance across the broadband spectrum, microring resonators are fabricated. For this work, air-cladded microring resonators with a 3-mm diameter (corresponding to a 21.2 GHz free spectral range) are used mostly for convenience in coupling and measurement, while also completely eliminating substrate leakage and bending losses (for details, see Supplementary Figs. 1 and 2). The microscopy image of a typical microring resonator is shown in Fig. 1d. The ring and pulley coupler are colorized in green, with ridge waveguides fabricated by etching trenches around the ridges to increase etch efficiency. Unlike Si_3N_4 photonic circuits, these PICs do not require stress release patterns even at 4 µm of thickness. The inherent low viscosity of Ge-silica can be accessed at standard furnace annealing temperatures, thereby allowing for surface-tension-induced smoothing. By choosing the appropriate temperature, the resonators can achieve atomic-scale smoothness without deformation of the waveguide shape (Fig. 1e). This smoothness overcomes the typical scattering limitations at short wavelengths in integrated microresonators.

U-shape tapered-fibre couplers[23] are used to measure *Q* factors from 458 nm to 1,550 nm. Intrinsic *Q* factors were determined from transmission spectra scans in the undercoupled regime (for some stronger coupled modes in the visible band, see Supplementary Fig. 5), in which resonant transmitted power and linewidth were used to infer loaded, coupled and intrinsic optical *Q* factors. A series of tunable external cavity lasers, each calibrated by a separate interferometer, were used to measure *Q* at each wavelength. Seven resonator transmission spectra at different wavelengths are shown in Fig. 1f, demonstrating intrinsic *Q* factors exceeding 180 million across a broad wavelength range

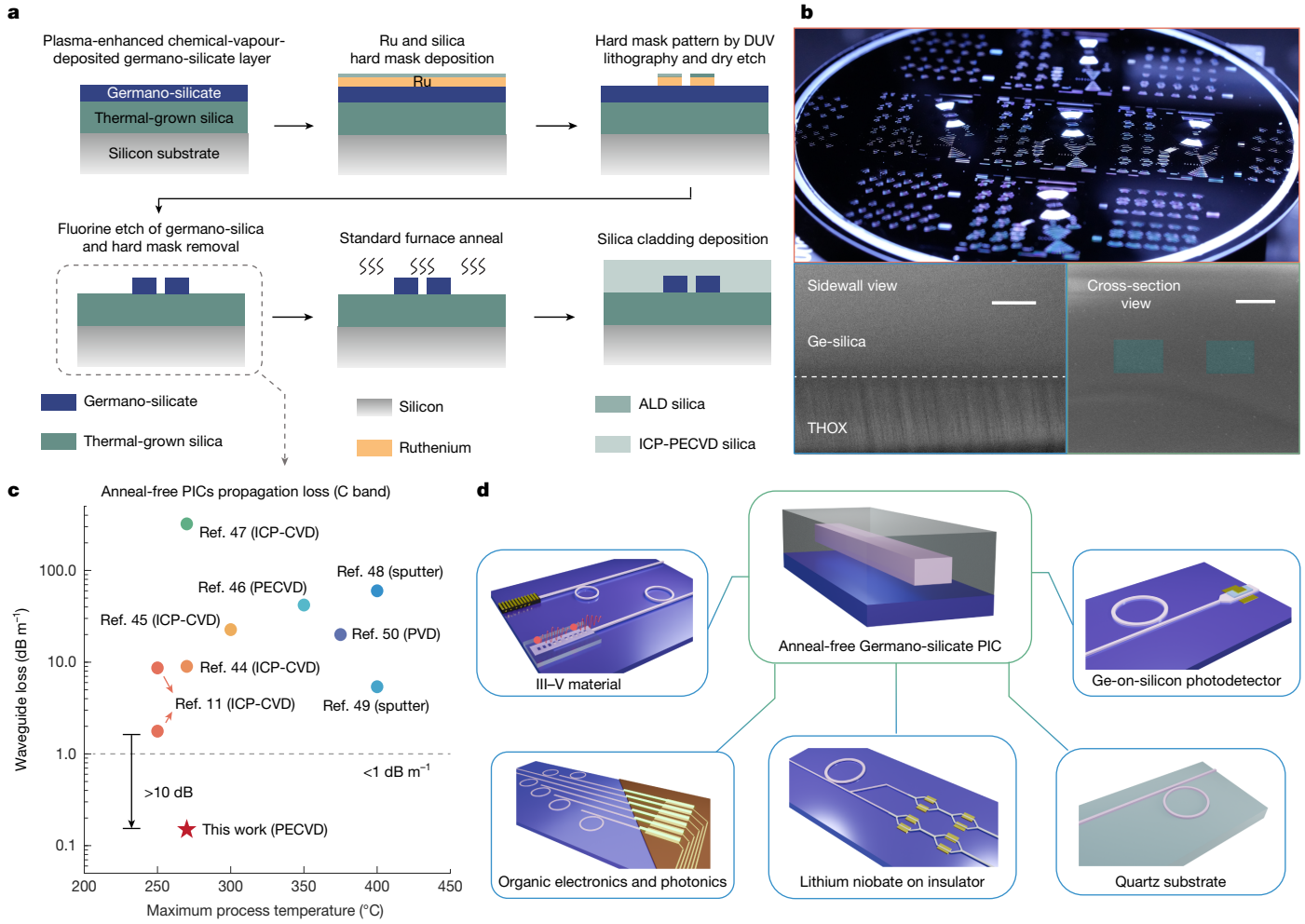

Fig. 2 | CMOS compatibility and process flow of Ge-silica ultralow-loss PICs. **a**, Schematic of fabrication workflow for ultrahigh-*Q* Ge-silica resonators. ALD, atomic layer deposition. **b**, Photograph of Ge-silica PICs on silicon at wafer scale, SEM image showing the sidewall of an annealed waveguide (intentionally overetched to show the contrast in reflow compared with non-reflowed material) and cross-section of cladded waveguides. **c**, Anneal-free waveguide loss (C band) compared with temperature for state-of-the-art low-loss PICs[11,44–50] compared with the present work. CVD, chemical vapour deposition; PVD, physical vapour deposition. **d**, Examples of monolithic/heterogeneous integration applications of ultralow-loss anneal-free Ge-silica PICs, including co-integration with III–V materials, organic electronics/photonics, thin-film lithium niobate, thermal-engineered quartz substrates and Ge-on-silicon photodetectors. Scale bars, 500 nm (**b**, bottom left); 5 µm (**b**, bottom right).

from 458 nm to 1,550 nm, with the highest *Q* of 463 million at 1,064 nm, corresponding to a waveguide loss of 0.08 dB m^{-1}. The waveguide loss α is calculated from resonators Q_0 by $\alpha(\mathrm{dB\ m^{-1}}) = 10 \times \log_{10}(e) \times \frac{2\pi n_{\mathrm{eff}}}{Q_0 \lambda}$. Here, n_{eff} is the effective index of optical modes and λ is the wavelength. The atomic-scale smoothness, along with the broad ultralow-material-loss window of Ge-silica, enables it to break the short-wavelength limitation and achieve the lowest waveguide propagation losses among all integrated platforms within the visible and short-NIR ranges (Fig. 1b). Notably, the loss at 458 nm is 0.49 dB m^{-1}, which is a 13-dB improvement over previous records.

CMOS-compatible fabrication

The fabrication process for this work is shown in Fig. 2a. In the devices studied, a 4-µm-thickness germano-silica layer (25 mol% GeO_2, corresponding to an approximately 2% refractive index difference) is deposited around 270 °C (setting the anneal-free thermal budget for the fabrication flow) by plasma-enhanced chemical vapour deposition (PECVD) on a thick (15 µm) layer of thermal oxide on silicon wafer. The Ge-silica layer is then processed into ridge waveguides through ruthenium (Ru) and silica hard masking[24], deep-ultraviolet (DUV) lithography and inductively coupled plasma etching. The Ru mask provides high selectivity in fluorine-based etches enabling high-fidelity deep etching of Ge:silica. To reduce the roughness-induced scattering loss limitation and achieve ultrahigh *Q* across the broadband spectrum, the entire wafer is subjected to furnace annealing at 1,000 °C for 12–18 h. As shown in Fig. 2b (bottom left), the sidewalls of the Ge-silica waveguides undergo reflow, removing the etch-induced roughness, whereas the thermally grown oxide (THOX) substrate remains unaffected.

From here, an optional upper silica cladding layer can be deposited. Two cladding deposition methods are investigated in this work and applied to different devices. First, a 14-µm thick slightly P-doped (1.5 mol% P_2O_5) silica cladding is used for full acoustic confinement (Fig. 2b, bottom right). Second, a higher-quality inductively coupled plasma PECVD (ICP-PECVD) is used to protect the devices from contamination and degradation due to long-term atmospheric exposure. With the addition of this ICP-PECVD >6 µm cladding (Extended Data Fig. 2a), the Ge-silica PICs have been confirmed to maintain ultralow loss (optical *Q* factors >10^8, as shown in Extended Data Fig. 2b), when exposed to the atmosphere for over several months.

Owing to the high quality of the PECVD Ge-silica layer, high precision of DUV lithography and the well-developed etching process[24],

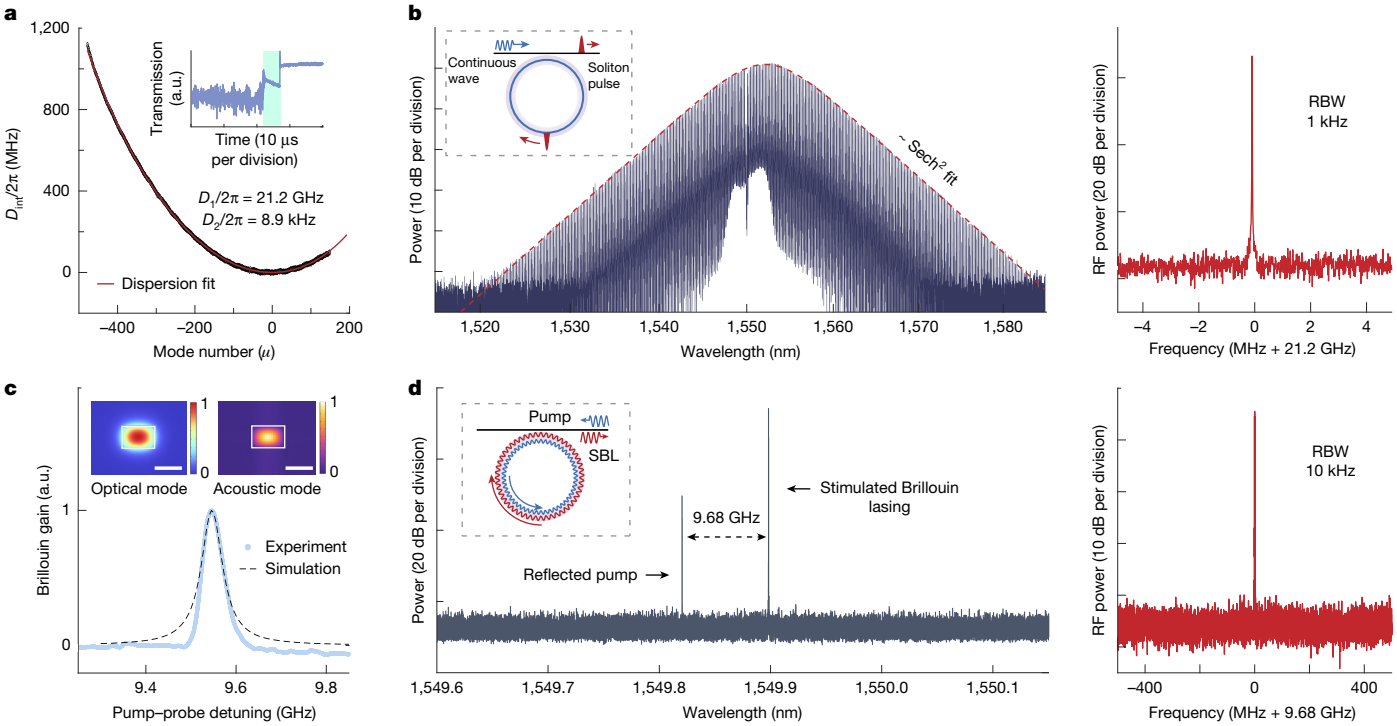

Fig. 3 | Demonstration applications using the germano-silicate platform. **a**, Dispersion of a Ge-silica single-ring resonator, $D_{int} = \omega_\mu - \omega_0 - D_1\mu$, where $\mu = 0$ is assigned to the mode at 1,550 nm, $D_1/2\pi$ is the mean free spectral range and D_2 is the group velocity dispersion (GVD) (positive for anomalous GVD). A fitting gives $D_1/2\pi$ = 21.2 GHz and $D_2/2\pi$ = 8.9 kHz. Inset, soliton step in transmission. **b**, Optical spectrum of generated soliton microcomb (left) and radiofrequency spectrum of microcomb beatnote (right). RBW, resolution bandwidth. **c**, Measured SBS gain spectrum of a fully cladded Ge-silica waveguide. The simulation result is overlaid on the measurement response. Insets, electric-field mode profile of the fundamental TE mode (left) and Brillouin-scattering induced displacement response (right). **d**, Optical spectrum of stimulated Brillouin laser (left) and radiofrequency spectrum of SBL beatnote (right). a.u., arbitrary units.

the Ge-silica microresonators can achieve ultrahigh Q even before annealing. Air-clad resonators without the reflow smoothing anneal are measured and attain ultrahigh Q of nearly 200 million and maintain ultrahigh Q across a similarly broad spectrum (Extended Data Fig. 1). This corresponds to a lowest waveguide loss of 0.15 dB m^{-1} at 1,550 nm. Figure 2c compares anneal-free waveguide loss (C band) of state-of-the-art integrated platforms with the present work, which exhibits a more than 10-fold reduction over the previous record. This anneal-free improvement in waveguide loss will enhance the performance of applications requiring co-integration with temperature-sensitive material such as III–V devices, organic electronics/photonics, thin-film lithium niobate, thermal-engineered quartz and Ge-on-silicon photodetectors (Fig. 2d).

Advantages and demonstrations

Beyond the ultralow loss across a broadband spectrum, the Ge-silica PICs have three more key advantages in dispersion engineering, acoustic confinement and thermal noise mitigation. To demonstrate them, soliton microcombs, stimulated Brillouin lasing (SBL) and SIL laser experiments are performed using the new platform. As these applications do not require monolithic or heterogeneous integration with other materials, annealed Ge:silica devices are used.

Single-ring soliton generation

Soliton microcombs represent the main new application area of microcavities and enable transfer of large-scale frequency comb technology to an integrated photonic chip. The Q factor of the microcavity determines the microcomb pumping power required as well as its coherence. However, at this time, the only ultrahigh-Q integrated platform—thin Si_3N_4—has a limited dispersion-engineering ability because of its thin waveguide thickness. This platform exhibits only normal dispersion and requires coupled-ring structures to generate soliton microcombs[25]. Here, an integrated Ge-silica resonator is used to demonstrate a new ability for an integrated design: soliton generation in a single ultrahigh-Q microring with anomalous dispersion. The microring resonator was designed to have anomalous dispersion and single-mode transmission as required for soliton generation (Supplementary Figs. 3 and 4). And the soliton mode family dispersion is characterized by measuring the frequency of all modes between 1,520 nm and 1,630 nm using an external cavity laser calibrated by a Mach–Zehnder interferometer (Fig. 3a). There is no observable mode-crossing-induced distortion of the mode family, therefore making the mode family well suited for soliton formation.

Soliton triggering and stabilization are performed using the frequency kick and capture-lock[26] technique. A measured soliton spectrum generated using a 3-mm-diameter ring is shown in Fig. 3b (for Q characterization, see Supplementary Fig. 6). The spectral envelope exhibits a well-defined sech^2 envelope. To confirm a stable repetition rate, the soliton pulse stream was detected and analysed using an electrical spectrum analyser. The electrical spectrum in Fig. 3b (right) gives a repetition rate near 21.2 GHz, and the resolution bandwidth of 1 kHz confirms pulse stream stability.

Acoustic confinement and Brillouin lasing

Apart from soliton microcombs, the stimulated Brillouin laser (SBL) is another device that has attracted considerable interest[27,28]. A key challenge for SBL operation is achieving simultaneous optical and acoustic waveguiding so as to enhance photon–phonon interactions—a feat hindered in conventional platforms by the low acoustic impedance of the silica cladding. Ge-silica PICs overcome this barrier through GeO_2 doping, which reduces the longitudinal acoustic velocity of the waveguide core relative to the silica cladding, thereby enabling a fully transverse confined acoustic mode.

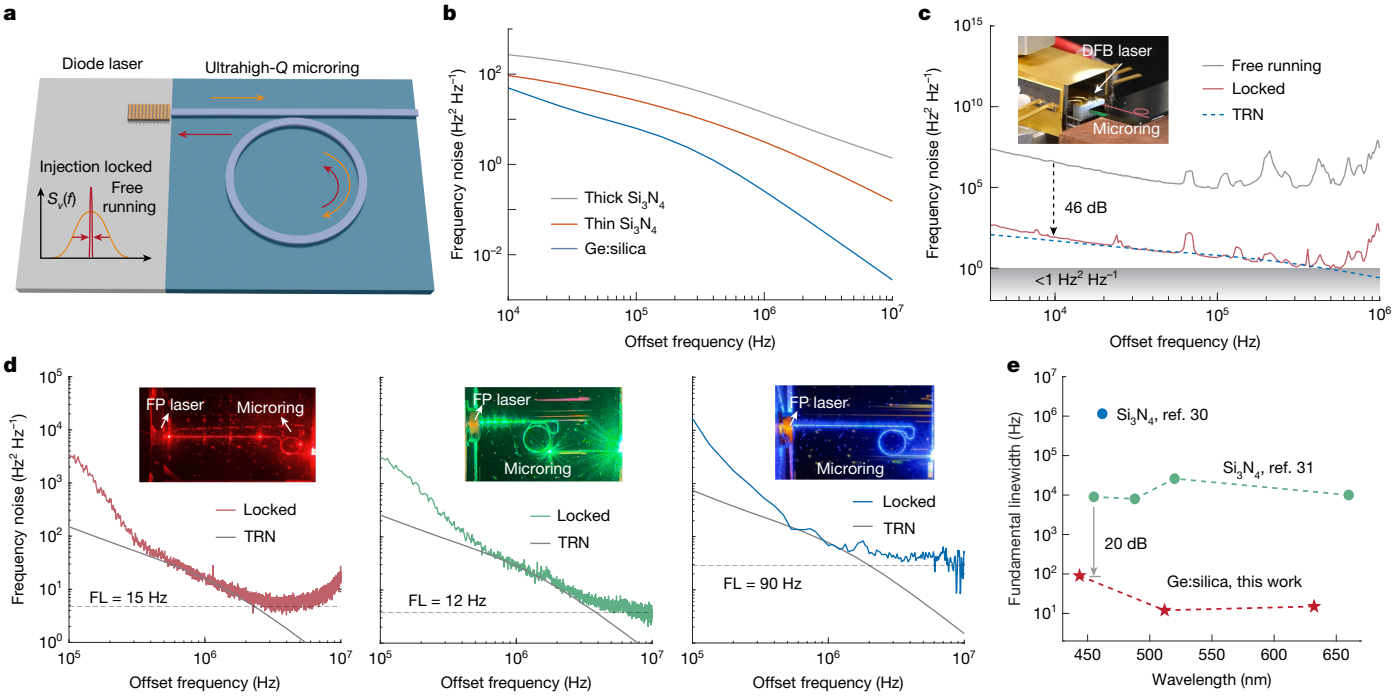

Fig. 4 | Hybrid integration of diode laser and germano-silicate device. **a**, Schematic of SIL of the diode laser using external ultrahigh-*Q* microring. **b**, Simulated TRN spectra. Mode areas are 28.06 μm², 7.71 μm² and 1.33 μm² for Ge-silica, thin Si_3N_4 and thick Si_3N_4, respectively. **c**, Single sideband frequency noise of SIL laser, indicating a Hz-level fundamental linewidth (FL). Inset, the image of a 1,550-nm DFB laser and integrated Ge-silica microring (indicated in false colour). **d**, Narrow-linewidth lasers at red, green and violet wavelengths, realized by SIL of Fabry–Pérot (FP) diode lasers to microrings. The fundamental linewidths are 15 Hz at 632 nm, 12 Hz at 512 nm and 90 Hz at 444 nm. **e**, Comparison of the fundamental linewidths of integrated lasers with state-of-the-art Si_3N_4 platforms[30,31].

In the experiment, an approximately 25-mm-long waveguide is used to characterize the stimulated Brillouin scattering (SBS) gain spectrum and verify acoustical confinement by comparison to simulation. The waveguide core is 4 μm × 6 μm Ge-silica, with 15-μm thermal silicon oxide bottom cladding and 14-μm P_2O_5-doped silica upper cladding (the same cladding as shown in Fig. 2b, bottom right). Simulations of the normalized electric field and mechanical displacement distributions, shown in Fig. 3c, demonstrate simultaneous optical and acoustic wave confinement. Applying a pump–probe method (Methods), the SBS gain spectrum is obtained and agrees well with the simulation. The gain peak at 9.55 GHz has a full width at half maximum of 44.7 MHz, corresponding to a mechanical quality factor of about 210.

As a device demonstration, integrated Ge-silica resonators are used to generate a high-coherence Brillouin laser. To achieve phase matching for the Brillouin process near 1,550 nm, air-clad devices with diameters of approximately 20 mm were fabricated (for *Q* characterization, see Supplementary Fig. 7). Figure 3d (left) shows the optical spectrum of the lasing Stokes wave. The weaker pump signal peak in the spectrum arises from the need to collect the lasing Stokes wave in the propagation direction opposite to the pumping direction. Its strength is determined by residual reflection and backscattering in the measurement. The Brillouin lasing frequency shift is 9.68 GHz, which is lower than the typical 10.9 GHz shift observed in silica resonators[18]. Figure 3d (right) shows the microwave beatnote between the pump and Stokes waves, revealing its high coherence, as indicated by the high signal-to-noise ratio. This synergy of ultralow optical loss and engineered acoustic confinement unlocks low-noise Brillouin lasers for high-performance on-chip gyroscopes[13], integrated microwave photonics and temperature/strain sensors.

LMA-enhanced hybrid-integrated low-noise laser

Narrow-linewidth lasers are pivotal for applications ranging from precision metrology to coherent optical communications. The recent integration of ultrahigh-*Q* microresonators with semiconductor diode lasers has markedly reduced the frequency noise of on-chip lasers and soliton microcombs by SIL[4]. The operational principle is shown in Fig. 4a. A resonant mode of the ultrahigh-*Q* microresonator acts as a frequency reference for stabilization, whereas backscattered light from the resonator provides optical feedback to narrow the linewidth of the diode laser. White frequency noise suppression scales quadratically with the quality factor (Q^2) of the microresonator, whereas TRN scales inversely with the cavity mode volume. Here, TRN in the resonator mode is simulated using the commercial finite element analysis software COMSOL Multiphysics (Methods). The results, plotted in Fig. 4b, compare Ge-silica with low- and high-confinement Si_3N_4 resonators of identical diameters. Calculated mode areas are 28.06 μm² (Ge-silica), 7.71 μm² (thin Si_3N_4) and 1.33 μm² (thick Si_3N_4). Owing to its substantially larger mode area, the Ge-silica platform has a greatly reduced TRN among the three integrated photonic systems.

As a demonstration of this hybrid-integrated low-noise laser based on our platform, a commercial C-band DFB laser is endfire-coupled to the bus waveguide of a Ge-silica resonator chip with *Q* factor exceeding 100 million (Fig. 4c, inset, in which the microring resonator and bus waveguide are indicated in false colour). The laser chip, which is mounted on a thermoelectric cooler to avoid long-term drift, is able to deliver power of >100 mW at 1,548 nm. Optical feedback is provided to the laser by backward Rayleigh scattering in the microresonator, which spontaneously aligns the laser frequency to the nearest resonator mode. In experiments, as the phase accumulated in the feedback is critical to determining the stability of injection locking, the feedback phase is controlled by adjusting the air gap between the chips. At a specific phase detuning, a soliton crystal comb[29] is generated (Supplementary Fig. 8a). The pump line of the comb output is filtered and directed to a self-heterodyne setup for frequency-noise characterization. The SIL operation boosts the laser coherence, with the frequency noise spectrum shown in Fig. 4c and achieves a Hz-level fundamental

linewidth resulting from a 46-dB noise reduction compared with the free-running DFB laser. In the data, the increasing frequency noise at high-offset frequency is an artefact of spontaneous noise from the DFB laser and can be eliminated by out-coupling from a drop waveguide[4].

The narrow-linewidth lasers are further extended into the visible spectrum by SIL of commercially available multimode Fabry–Pérot diode lasers to high-*Q* microrings. Under SIL, the devices become single mode with high side-mode-suppression ratios (Supplementary Fig. 8b). Also, fundamental linewidths of 15 Hz at 632 nm, 12 Hz at 512 nm and 90 Hz at 444 nm are achieved (Fig. 4d). Compared with state-of-the-art integrated lasers[30,31], the Ge:silica platform provides more than 20 dB improvement in fundamental linewidth across the visible spectrum (Fig. 4e), holding the potential to redefine performance benchmarks in integrated visible photonics[14].

Discussion

In summary, we have developed a Ge-silica ultralow-loss platform that markedly advances integrated photonics (see detailed comparison between Ge-silica and the state-of-the-art low-loss Si_3N_4 in Supplementary Table 1). This new platform has achieved a >10 dB improvement in both the violet wavelength range and anneal-free *Q*. The unique material and geometric properties of these waveguides enable dispersion engineering for soliton microcomb generation, simultaneous confinement of acoustic and optical modes, and suppression of thermal refractive noise. They also maintain ultrahigh *Q* factors in both polarizations, and enhance power-handling abilities for high-power mode-locked lasers. Moreover, the photosensitivity of Ge-silica[32] allows UV-written optical gratings for applications forming the basis of fibre Bragg gratings in photonic systems. By contrast, the small index contrast of Ge:silica on silica leads to larger bending losses, which limit integration density. These can be mitigated by using 3D integration, increasing Ge doping or operating at shorter wavelengths. On account of the quadratic[33] and cubic dependence[34] of nonlinearity on optical *Q* factor, the low nonlinearity of silica can be readily compensated by exploiting ultrahigh-*Q* devices. Moreover, electro-optic tuning can be enabled through heterogeneous integration with lithium niobate or lithium tantalate.

The surface-tension-induced smoothness of the waveguides bypasses Rayleigh scattering loss limitations, greatly extending integrated photonics at shorter operational wavelengths. Specifically, by integrating visible diode lasers with ultralow-loss Ge-silica resonators, Hz-level, narrow-linewidth lasers[31] and microcombs[35] are possible in the visible band. With further development in deposition and fabrication techniques, the Ge-silica PICs hold the potential to reach their material-limited waveguide loss of 0.2 dB km^{-1} (corresponding to a microresonator *Q* factor of >100 billion). This fibre-like optical loss for PICs would revolutionize certain fibre-based technologies by moving their manufacture to CMOS foundries, including solid-state gyroscopes, advanced frequency comb technology for precision portable clocks, large-scale low-loss circuits for quantum computing, high-power amplifiers and mode-locked lasers.

Online content

Any methods, additional references, Nature Portfolio reporting summaries, source data, extended data, supplementary information, acknowledgements, peer review information; details of author contributions and competing interests; and statements of data and code availability are available at https://doi.org/10.1038/s41586-025-09889-w.

1. Burmeister, E. F. et al. Photonic integrated circuit optical buffer for packet-switched networks. *Opt. Express* **17**, 6629–6635 (2009).
2. Bauters, J. F. et al. Planar waveguides with less than 0.1 dB/m propagation loss fabricated with wafer bonding. *Opt. Express* **19**, 24090–24101 (2011).
3. Liu, J. et al. High-yield, wafer-scale fabrication of ultralow-loss, dispersion-engineered silicon nitride photonic circuits. *Nat. Commun.* **12**, 2236 (2021).
4. Jin, W. et al. Hertz-linewidth semiconductor lasers using CMOS-ready ultra-high-Q microresonators. *Nat. Photon.* **15**, 346–353 (2021).
5. Spencer, D. T. et al. An optical-frequency synthesizer using integrated photonics. *Nature* **557**, 81–85 (2018).
6. Kudelin, I. et al. Photonic chip-based low-noise microwave oscillator. *Nature* **627**, 534–539 (2024).
7. Riemensberger, J. et al. Massively parallel coherent laser ranging using a soliton microcomb. *Nature* **581**, 164–170 (2020).
8. Feng, H. et al. Integrated lithium niobate microwave photonic processing engine. *Nature* **627**, 80–87 (2024).
9. Chauhan, N. et al. Ultra-low loss visible light waveguides for integrated atomic, molecular, and quantum photonics. *Opt. Express* **30**, 6960–6969 (2022).
10. Corato-Zanarella, M., Ji, X., Mohanty, A. & Lipson, M. Absorption and scattering limits of silicon nitride integrated photonics in the visible spectrum. *Opt. Express* **32**, 5718–5728 (2024).
11. Bose, D. et al. Anneal-free ultra-low loss silicon nitride integrated photonics. *Light Sci. Appl.* **13**, 156 (2024).
12. Newman, Z. L. et al. Architecture for the photonic integration of an optical atomic clock. *Optica* **6**, 680–685 (2019).
13. Lai, Y.-H. et al. Earth rotation measured by a chip-scale ring laser gyroscope. *Nat. Photon.* **14**, 345–349 (2020).
14. Lu, X. et al. Emerging integrated laser technologies in the visible and short near-infrared regimes. *Nat. Photon.* **18**, 1010–1023 (2024).
15. Tran, M. A. et al. Extending the spectrum of fully integrated photonics to submicrometre wavelengths. *Nature* **610**, 54–60 (2022).
16. Pedersen, A. T., Grüner-Nielsen, L. & Rottwitt, K. Measurement and modeling of low-wavelength losses in silica fibers and their impact at communication wavelengths. *J. Lightwave Technol.* **27**, 1296–1300 (2009).
17. Armani, D., Kippenberg, T., Spillane, S. & Vahala, K. Ultra-high-Q toroid microcavity on a chip. *Nature* **421**, 925–928 (2003).
18. Lee, H. et al. Chemically etched ultrahigh-Q wedge-resonator on a silicon chip. *Nat. Photon.* **6**, 369–373 (2012).
19. Himeno, A., Kato, K. & Miya, T. Silica-based planar lightwave circuits. *IEEE J. Sel. Top. Quantum Electron.* **4**, 913–924 (1998).
20. Birtch, E. M., Shelby, J. E. & Marc Whalen, J. Properties of binary GeO_2-SiO_2 glasses. *Phys. Chem. Glasses: Eur. J. Glass Sci. Technol. B* **47**, 182–185 (2006).
21. Kao, C. K. Nobel lecture: Sand from centuries past: Send future voices fast. *Rev. Mod. Phys.* **82**, 2299–2303 (2010).
22. Niffenegger, R. J. et al. Integrated multi-wavelength control of an ion qubit. *Nature* **586**, 538–542 (2020).
23. Dong, C-H. et al. Coupling of light from an optical fiber taper into silver nanowires. *Appl. Phys. Lett.* **95**, 221109 (2009).
24. Mitchell, W. J., Thibeault, B. J., John, D. D. & Reynolds, T. E. Highly selective and vertical etch of silicon dioxide using ruthenium films as an etch mask. *J. Vac. Sci. Technol. A* **39**, 043204 (2021).
25. Yuan, Z. et al. Soliton pulse pairs at multiple colours in normal dispersion microresonators. *Nat. Photon.* **17**, 977–983 (2023).
26. Yi, X., Yang, Q.-F., Yang, K. Y. & Vahala, K. Active capture and stabilization of temporal solitons in microresonators. *Opt. Lett.* **41**, 2037–2040 (2016).
27. Otterstrom, N. T., Behunin, R. O., Kittlaus, E. A., Wang, Z. & Rakich, P. T. A silicon Brillouin laser. *Science* **360**, 1113–1116 (2018).
28. Eggleton, B. J., Steel, M. J. & Poulton, C. G.*Brillouin Scattering Part 2*, 1st edn, Vol. 110 (Academic Press, 2022).
29. Lu, Z. et al. Synthesized soliton crystals. *Nat. Commun.* **12**, 3179 (2021).
30. Siddharth, A. et al. Near ultraviolet photonic integrated lasers based on silicon nitride. *APL Photon.* **7**, 046108 (2022).
31. Corato-Zanarella, M. et al. Widely tunable and narrow-linewidth chip-scale lasers from near-ultraviolet to near-infrared wavelengths. *Nat. Photon.* **17**, 157–164 (2023).
32. Hill, K. O., Fujii, Y., Johnson, D. C. & Kawasaki, B. S. Photosensitivity in optical fiber waveguides: Application to reflection filter fabrication. *Appl. Phys. Lett.* **32**, 647–649 (1978).
33. Kippenberg, T. J., Spillane, S. M. & Vahala, K. J. Kerr-nonlinearity optical parametric oscillation in an ultrahigh-Q toroid microcavity. *Phys. Rev. Lett.* **93**, 083904 (2004).
34. Carmon, T. & K, V. Visible continuous emission from a silica microphotonic device by third-harmonic generation. *Nat. Phys.* **3**, 430–435 (2007).
35. Chen, H.-J. et al. Chaos-assisted two-octave-spanning microcombs. *Nat. Commun.* **11**, 2336 (2020).
36. Morin, T. J. et al. CMOS-foundry-based blue and violet photonics. *Optica* **8**, 755–756 (2021).
37. Isichenko, A. et al. Sub-Hz fundamental, sub-kHz integral linewidth self-injection locked 780 nm hybrid integrated laser. *Sci. Rep.* **14**, 27015 (2024).
38. Liu, P. et al. Near-visible integrated soliton microcombs with detectable repetition rates. *Nat. Commun.* **16**, 4780 (2025).
39. Lu, X. et al. Milliwatt-threshold visible–telecom optical parametric oscillation using silicon nanophotonics. *Optica* **6**, 1535–1541 (2019).
40. Karpov, M., Pfeiffer, M. H. P., Liu, J., Lukashchuk, A. & Kippenberg, T. J. Photonic chip-based soliton frequency combs covering the biological imaging window. *Nat. Commun.* **9**, 1146 (2018).
41. Desiatov, B., Shams-Ansari, A., Zhang, M., Wang, C. & Lončar, M. Ultra-low-loss integrated visible photonics using thin-film lithium niobate. *Optica* **6**, 380–384 (2019).
42. Renaud, D. et al. Sub-1 Volt and high-bandwidth visible to near-infrared electro-optic modulators. *Nat. Commun.* **14**, 1496 (2023).
43. Sund, P. I. et al. High-speed thin-film lithium niobate quantum processor driven by a solid-state quantum emitter. *Sci. Adv.* **9**, eadg7268 (2023).
44. Xie, Y. et al. Soliton frequency comb generation in CMOS-compatible silicon nitride microresonators. *Photon. Res.* **10**, 1290–1296 (2022).

45. Chiles, J. et al. Deuterated silicon nitride photonic devices for broadband optical frequency comb generation. *Opt. Lett.* **43**, 1527–1530 (2018).
46. Ji, X. et al. Ultra-low-loss silicon nitride photonics based on deposited films compatible with foundries. *Laser Photon. Rev.* **17**, 2200544 (2023).
47. Chia, X. X. et al. Low-power four-wave mixing in deuterated silicon-rich nitride ring resonators. *J. Lightwave Technol.* **41**, 3115–3130 (2023).
48. Frigg, A. et al. Low loss CMOS-compatible silicon nitride photonics utilizing reactive sputtered thin films. *Opt. Express* **27**, 37795–37805 (2019).
49. Zhang, S. et al. Low-temperature sputtered ultralow-loss silicon nitride for hybrid photonic integration. *Laser Photon. Rev.* **18**, 2300642 (2024).
50. Golshani, N. et al. Low-loss, low-temperature PVD SiN waveguides. In *Proc. IEEE 17th Int. Conf. Group IV Photonics (GFP)*, 1–2 (IEEE, 2021).

Publisher's note Springer Nature remains neutral with regard to jurisdictional claims in published maps and institutional affiliations.

Open Access This article is licensed under a Creative Commons Attribution-NonCommercial-NoDerivatives 4.0 International License, which permits any non-commercial use, sharing, distribution and reproduction in any medium or format, as long as you give appropriate credit to the original author(s) and the source, provide a link to the Creative Commons licence, and indicate if you modified the licensed material. You do not have permission under this licence to share adapted material derived from this article or parts of it. The images or other third party material in this article are included in the article's Creative Commons licence, unless indicated otherwise in a credit line to the material. If material is not included in the article's Creative Commons licence and your intended use is not permitted by statutory regulation or exceeds the permitted use, you will need to obtain permission directly from the copyright holder. To view a copy of this licence, visit http://creativecommons.org/licenses/by-nc-nd/4.0/.

© The Author(s) 2026, modified publication 2026

Methods

High-quality upper silica cladding deposition

The upper cladding of these germano-silicate resonators was deposited by ICP-PECVD (Unaxis VLR) at 250 °C using a deuterated silane based precursor and oxygen plasma. To reduce the losses due to the stress optic effect of the cladding, while also repairing the solarization of the germano-silicate due to direct plasma exposure, the devices studied underwent a 20-min 1,000 °C rapid thermal anneal between each deposition of 500 nm of cladding. As a test, we deposited a 6-µm thickness upper cladding (Extended Data Fig. 2a), observing complete filling of the coupling gap. This encapsulation effectively protects the device from environmental contamination, enabling the maintenance of ultrahigh Q up to 160 million (Extended Data Fig. 2b) over several months. It is noted that the original Q factor before cladding deposition was measured at approximately 250 million. This decrease in Q factor with upper cladding, partial Q recovery through thermal treatment, yet never fully recovering the original Q values, is consistent with what was previously observed in ULL silicon nitride in ref. 51, in which the same ICP-PECVD system was used. The possible solutions to this would be to switch to a deposition type that avoids exposure to a plasma or using better precursors, such as low-pressure chemical vapour deposition or tetraethoxysilane PECVD[52].

Brillouin gain spectrum measurements and simulations

To achieve high sensitivity, we use a dual-intensity-modulation pump–probe technique[53]. The test device has a 14-µm-thick 1.5 mol% P_2O_5-doped silica upper cladding, designed to fully confine both optical and acoustic fields. This slightly phosphorus-doped silica layer was deposited by PECVD, chosen for its ability to rapidly produce thick, stress-free films. Post-cladding characterization shows waveguide propagation loss below 0.5 dB m^{-1} and edge coupling loss of 1.4 dB per facet. The SBS gain characterization uses counterpropagating pump and probe lasers injected through facet couplers, with both lasers operating near 1,560 nm. The pump laser is intensity-modulated at a frequency of 10 MHz and the probe laser is intensity-modulated at a frequency of 10.075 MHz. The transmission signal of the probe laser is routed to a lock-in amplifier for gain measurement, using a 75-kHz reference beatnote of the two modulation frequencies. The SBS gain spectrum is obtained by frequency-scanning the probe laser over a 20 GHz range from red- to blue-detuning relative to the fixed pump frequency. Both optical and acoustic fields are calculated using the finite element method based on the model described in ref. 54. The material properties used in the simulation are as follows: refractive index of 1.478, 1.451 and 1.449; density of 2,750, 2231 and 2,200 kg m^{-3}; Poisson's ratio of 0.180, 0.166 and 0.170; Young's modulus of 64.8, 72.6 and 73.0 GPa; Brillouin linewidth of 59 MHz, 28 MHz and 17 MHz; and photoelastic coefficient p_{12} of 0.2373, 0.2264 and 0.2260, for Ge-silica (core), P-silica (upper cladding) and thermally grown silica (bottom cladding), respectively.

TRN simulations

The TRN in Fig. 4b of Ge-silica, thin SiN and thick SiN are numerically simulated in a finite element solver (COMSOL Multiphysics) using a model based on the fluctuation-dissipation theorem[55]. For each of the three materials, the simulation is based on a ring microresonator with a diameter of 3 mm. The rectangular waveguide dimensions of the Ge-silica, thin SiN and thick SiN microresonators are 12 µm × 4 µm, 8 µm × 0.1 µm and 2 µm × 0.8 µm, respectively (width × height). These dimensions of thin SiN and thick SiN are taken from refs. 4,56. The Ge-silica waveguide is air-cladded, whereas the thin and thick SiN waveguides have silica cladding. Material parameters used in the simulation are as follows: for Ge-silica, the thermo-optic coefficient 1.27×10^{-5} K^{-1}, heat conductivity 1.38 W m^{-1} K^{-1}, heat capacity 740 J kg^{-1} K^{-1}, density 2.2×10^3 kg m^{-3}; for SiN, the thermo-optic coefficient 2.45×10^{-5} K^{-1}, heat conductivity 30 W m^{-1} K^{-1}, heat capacity 800 J kg^{-1} K^{-1}, density 3.29×10^3 kg m^{-3}; for the silica cladding of the SiN waveguide, the thermo-optic coefficient 1.2×10^{-5} K^{-1}, heat conductivity 1.38 W m^{-1} K^{-1}, heat capacity 740 J kg^{-1} K^{-1}, density 2.2×10^3 kg m^{-3}. The ambient temperature is set at 300 K.

Data availability

The data presented in the main text are available from Zenodo[57]. All other data are available from the corresponding authors upon request.

Code availability

The codes used in the study are available from the corresponding authors upon request.

51. Guo, J. et al. Investigation of Q degradation in low-loss Si_3N_4 from heterogeneous laser integration. *Opt. Lett.* **49**, 4613–4616 (2024).
52. Liu, K. et al. Ultralow 0.034 dB/m loss wafer-scale integrated photonics realizing 720 million Q and 380 µW threshold Brillouin lasing. *Opt. Lett.* **47**, 1855–1858 (2022).
53. Botter, R. et al. Guided-acoustic stimulated brillouin scattering in silicon nitride photonic circuits. *Sci. Adv.* **8**, eabq2196 (2022).
54. Qiu, W. et al. Stimulated Brillouin scattering in nanoscale silicon step-index waveguides: a general framework of selection rules and calculating SBS gain. *Opt. Express* **21**, 31402–31419 (2013).
55. Kondratiev, N. M. & Gorodetsky, M. Thermorefractive noise in whispering gallery mode microresonators: analytical results and numerical simulation. *Phys. Lett. A* **382**, 2265–2268 (2018).
56. Huang, G. et al. Thermorefractive noise in silicon-nitride microresonators. *Phys. Rev. A* **99**, 061801 (2019).
57. Chen, H.-J., Colburn, K. et al. Data for "Towards fibre-like-loss for photonic integration from violet to near-IR". *Zenodo* https://doi.org/10.5281/zenodo.17478213 (2025).

Acknowledgements This work was funded by DARPA (HR0011-22-2-0009 and HR00112420383), the Air Force Research Laboratory (FA9453-20-2-0001), the EPSRC grant (EP/Z531169/1) and the Kavli Nanoscience Institute (KNI) at Caltech. K.C. thanks the NSF for graduate fellowship support (2139433). We acknowledge the support of the entire UCSB Nanofabrication facility and its staff (especially D. John, B. Thibeault, B. Mitchell and D. Read), the Caltech KNI staff (K. McKenzie), as well as I. Hedgepeth, B. Moog, K. Liu, Q.-F. Yang, J. Guo, M. Li, L. Wu and J. Bowers. We thank the helpful discussion with X. Yin from S. H. Xinguang Optoelectronics Technology, Y. Huang from Henan Shijia Photons Technology and X. Shi and X. Fu from Shanghai Precilasers Technology.

Author contributions H.-J.C., K.C., H.B. and K.V. conceived the idea and designed the experiments. H.-J.C. and K.C. developed, fabricated and characterized the devices. P. Lehan assisted in the fabrication of the devices. P. Liu, H.Y., H.H. and J.-Y.L. simulated and/or designed the circuits. H.-J.C., K.C., H.H., P. Liu and J. Ge performed the measurements and experiments, with assistance from Q.-X.J., Z.Y. and H.Y.; C.H. and J. Gates provided valuable discussions on the Ge:silica platform development. D.B. hosted and contributed instruments for part of the experiments. H.-J.C., K.C. and K.V. wrote the paper with assistance from all other authors.

Competing interests The authors declare no competing interests.

Additional information

Supplementary information The online version contains supplementary material available at https://doi.org/10.1038/s41586-025-09889-w.

Correspondence and requests for materials should be addressed to Hao-Jing Chen, Kellan Colburn or Kerry Vahala.

Peer review information *Nature* thanks Martino Bernard, Mher Ghulinyan and the other, anonymous, reviewer(s) for their contribution to the peer review of this work.

Reprints and permissions information is available at http://www.nature.com/reprints.

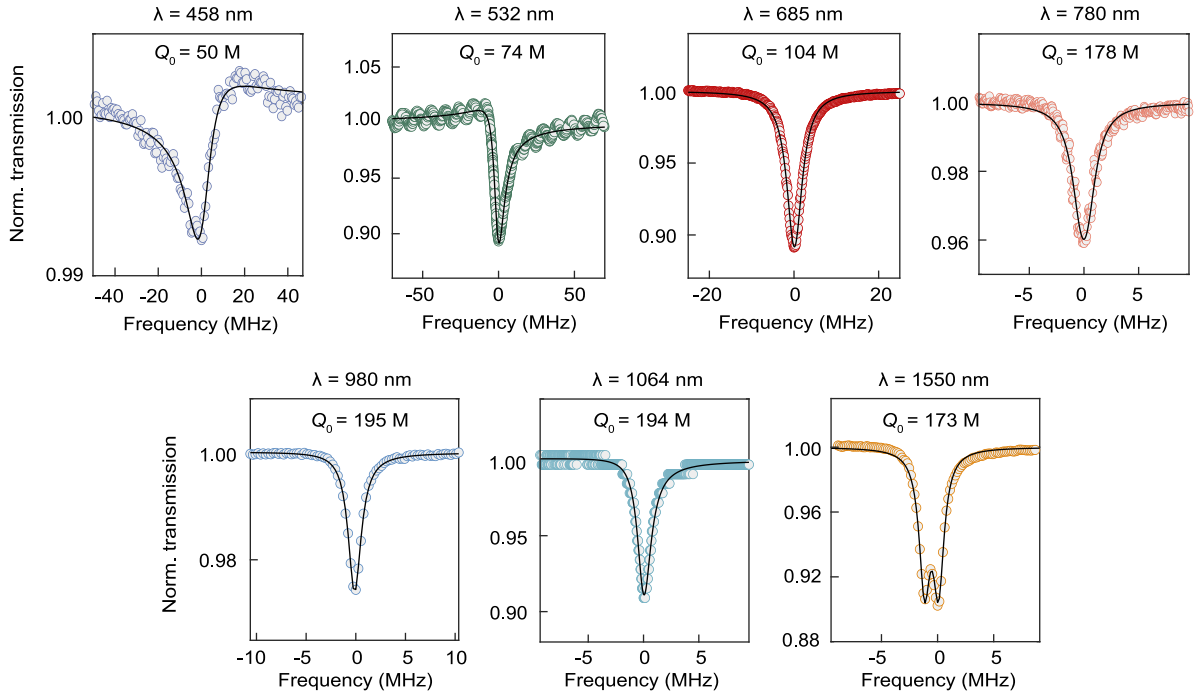

Extended Data Fig. 1 | Anneal-free microresonator characterization. Resonator transmission spectra and corresponding intrinsic *Q* factors (Q_0) of anneal-free Ge-silica microring resonators at 7 wavelengths, which are 50M at 458 nm, 74M at 532 nm, 104M at 685 nm, 178M at 780 nm, 195M at 980 nm, 194M at 1064 nm, and 173M at 1550 nm, respectively. Corresponding waveguide loss of 1.76 dB/m at 458 nm, 1.02 dB/m at 532 nm, 0.56 dB/m at 685 nm, 0.29 dB/m at 780 nm, 0.21 dB/m at 980 nm, 0.19 dB/m at 1064 nm, 0.15 dB/m at 1550 nm.

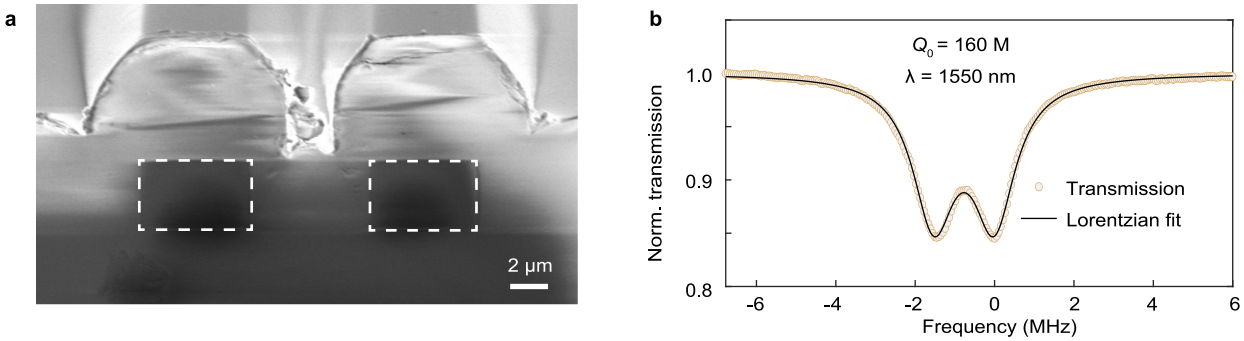

Extended Data Fig. 2 | Cladded germano-silicate PIC. a, SEM image of a cladded device deposited by 6 µm thickness ICP-PECVD silica. **b**, Transmission spectrum of a fully cladded resonator, indicating an intrinsic Q factor (Q_0) of 160M at 1550 nm.